Numerical Setup and Boundary Conditions

The 3-D computational domain is 2000 km long, 200 km wide, and 200 km deep (Fig. DR1a). This domain represents the lithosphere and upper asthenosphere across a passive margin (straight or curved), in the middle of the model, with a continent/ocean boundary dipping 45º toward the continent. The model resolution was 2 km everywhere.

The lithospheric structure in the present models is similar to that used in Nikolaeva et al. (2011) for the SE Brazilian margin. The oceanic domain does not initially include sediments, but sediments fill the trench after its arcward slope reaches a critical angle of 17° and prescribed erosion takes place. The material properties and used parameters are listed in Tables DR1 and DR2. The model geometry, particularly for the ocean-continent transition depicted in Figure DR1a, is based on the conceptual model for passive margin generation (e.g., Whitmarsh et al., 2001). According to this model, an initial asthenospheric upwelling during break-up leads to thinning of the overlying lower continental crust before the breakup of the continent. As the asthenosphere continues to ascend it undergoes decompression melting, which results in the formation of oceanic lithosphere and subsequent seafloor spreading. The boundary between the oceanic and continental lithosphere thus dips toward the continent.

The temperature structure of the model lithosphere is controlled by its thickness and is defined by a linear profile from 0 ºC at the surface to a prescribed temperature at the base of the lithosphere. The initial temperature gradient in the asthenospheric mantle was 0.5 °C km^{-1}.

The velocity boundary conditions are free slip at the top ($Y = 0$), and at the front and back boundaries ($Z = 0$ and 200 km). The left and right boundaries are fixed. For the permeable lower boundary condition (e.g., Burg and Gerya, 2005; Gerya et al., 2008; Li et al., 2010), an external outflux boundary implies constant normal velocity and zero shear stress conditions to be satisfied at ~200 km below the base of the model domain. The external boundary condition allows global conservation of mass in the computational domain and is implemented by using a limitation for velocity components at the lower boundary.

We imposed an internal erosion/sedimentation surface at the top of both plates by using a 10 km thick top layer of “sticky air” with a low density (1 kg m^{-3}) and viscosity of 10^{18} Pa s. A 4 km thick layer of “sticky sea water” (density = 1000 kg m^{-3}, viscosity = 10^{18} Pa s) is located between the oceanic lithosphere and the “sticky air” layer. The large viscosity contrast between the “sticky” layers and lithosphere minimizes shear stresses (< 104 Pa) across their interface, allowing the surface of the lithosphere to behave essentially as a free surface. The validity of the weak layer approach for approximating the free surface was recently benchmarked using a large variety of numerical techniques (Schmeling et al., 2008) (including the I3ELVIS code used here) and compared with analogue models.

Fluid/Melt Transport Mechanism

In order to simulate the migration of water released by dehydration, we used independently moving rock and fluid markers (Gorczyk et al., 2007). The maximum stable water content for each lithology was calculated by free energy minimization (Connolly, 2005)

as a function of pressure and temperature from thermodynamic data by the Perple_X program (Connolly, 2005; Gerya et al., 2006). The initial water content is zero everywhere, except in the basaltic and sedimentary crust where, in addition to mineralogical water, a porous water content is specified as a linear function of depth:

$$X_{H_2O(p)}(wt\%) = X_{H_2O(p_0)}(1 - 0.013\Delta y) \quad (1)$$

where $X_{H_2O(p_0)}$ = 2 wt% is the porous water content at the surface, and Δy is the depth below the surface in km (0–75 km). The subsequent release of this water also mimics the effects of low-temperature (< 300 °C) reactions that are not included in our thermodynamic database.

A fluid marker with a particular water amount is generated when the local water concentration exceeds the maximum concentration that can be held, and moves upwards until it reaches a lithology that assimilates water. Up to 2 wt% of water can be absorbed by hydrated mantle under supersolidus conditions, in agreement with seismic constraints (Bostock et al., 2002; Carlson and Miller, 2003). Solid mantle that could melt with the addition of water can absorb a maximal bulk water content of 0.5 wt%, consistent with typical conditions of fluid-fluxed melting in subduction zones (Kelley et al., 2006).

The velocity of water in the wedge is computed according to pressure gradients (e.g., Faccenda et al., 2009, 2012) as:

$$\begin{aligned} v_{x(water)} &= v_x - A\frac{\partial P}{\partial x} \\ v_{z(water)} &= v_z - A\frac{\partial P}{\partial z} \\ v_{y(water)} &= v_y - A(\frac{\partial P}{\partial y} - \rho_{fluid} g_y) \\ A &= \frac{v_{percolation}}{g_z(\rho_{mantle} - \rho_{fluid})} \end{aligned} \quad (2)$$

where y is the vertical coordinate, and x and z are respectively horizontal and lateral (along strike) coordinates (Fig. DR1); v_x, v_y and v_z indicate the local velocity of the solid mantle; A is a water percolation constant; $v_{percolation} = 10$ cm/yr is a pre-assumed standard water percolation velocity, which is in the range of the typical large-scale water transport velocities (1–10 cm/yr) in the mantle wedge (e.g. Peacock, 1990; Gorczyk et al., 2007; Nikolaeva et al., 2008); g_y = 9.81 m/s^2 is the gravitational acceleration; ρ_{mantle} = 3300 kg/m^3 and ρ_{fluid} = 1000 kg/m^3 are the densities of the mantle and fluid, respectively. The moving water is consumed by hydration and melting reactions with the mantle located atop the slab.

When the amount of melt reaches the melt extraction threshold, a very fast upward melt migration rate is assumed in all models (e.g., Hawkesworth et al., 1997; Hall and Kincaid, 2001; Nikolaeva et al., 2008; Hebert et al., 2009; Connolly et al., 2009). This instantaneous upward melt movement assumption does not account for lateral melt percolation phenomena driven by horizontal pressure gradients (e.g., Spiegelman and McKenzie, 1987). In a simple way, extracted melt is assumed to be instantaneously removed from the source region to the surface as extrusive volcanics, without considering its emplacement underneath the continental crust (Gerya and Meilick, 2011; Vogt et al., 2012). Also, similarly to Nikolaeva et al. (2008), we concentrate on fluid-fluxed melting processes

atop the slab, and do not model shallow decompression melting of the dry mantle under back-arc spreading centers.

Partial Melting and Melt Extraction

The degree of melting of hydrated peridotite is computed as a function of pressure, temperature and water content using the parameterization of Katz et al. (2003). The degree of melting of subducted crustal rocks is calculated according to the simpler linear melting model (Gerya and Yuen, 2003; Zhu et al., 2009, 2011):

$$\begin{aligned} &M_0 = 0 \text{ at } T<T_{solidus} \\ &M_0 = (T-T_{solidus})/(T_{liquidus}-T_{solidus}) \ \ at\ T_{solidus}<T<T_{liquidus} \\ &M_0 = 1 \text{ at } T>T_{liquidus} \end{aligned} \qquad (3)$$

where M_0 is the volumetric fraction of melt with temperature T; $T_{solidus}$ and $T_{liquidus}$ are, respectively, the solidus temperature (wet and dry solidi are used for the hydrated and dry mantle respectively) and the dry liquidus temperature (see Table 1 in Zhu et al., 2013).

For model simplicity, the melt extraction threshold in our model is the same for all types of melt. Although it can be lower for low-viscosity basaltic melts, it can be notably higher for the more viscous granitic and dacitic melts present in our models. Faul (2001) has shown that a deep, volatile-rich melt with low viscosity and density is mobile at 0.1% porosity, but basaltic melt only becomes mobile at a porosity above 1%. Nikolaeva et al. (2008) varied melt extraction threshold from 0.2 to 30% melt fraction to find its influence on crust production. Here we use an intermediate value for the melt extraction threshold M_{max} of 4% or 6%, and a non-extractable melt fraction (that remains in the source region) M_{min} of 2% or 3%, similar to previous 2-D models (Nikolaeva et al., 2008; Gerya and Meilick, 2011; Vogt et al., 2012). The amount of melt extraction is tracked by markers during the evolution of each experiment. In order to avoid over-extraction of melts from the moving rock markers, and keep non-extractable melt in the mantle, the total amount of available melt M for every marker takes into account previously extracted melt, and is calculated as:

$$M = M_0 - \sum_n M_{ext} \qquad (4)$$

where $\sum_n M_{ext}$ is the total melt fraction extracted during the previous n extraction episodes. In our model, the rock is considered non-molten (refractory) when the extracted melt fraction is larger than the standard one (i.e., when $\sum_n M_{ext} > M_0$). When the total amount of melt M exceeds the threshold $M_{\max}$, the melt fraction $M_{ext} = M - M_{\min}$ is extracted and $\sum_n M_{ext}$ is updated. After each melt extraction episode, only non-extractable melt remains in the source region ($M = M_{min}$). Starting from this moment, the total amount of melt M in the source region varies dynamically according to (4) and (5), until it again reaches the $M_{\max}$ threshold and another melt extraction episode takes place, as is schematically presented (Zhu et al., 2013). The extracted melt fraction M_{ext} is assumed to propagate upward to the surface much faster than the mantle rocks deform (Elliott et al., 1997; Hawkesworth et al., 1997). Hence, the instantaneous transmission of extracted melt to the surface is reasonable. At the surface, extracted melt markers create a volcanic arc and thereby retain their volume and composition. The effective density ρ_{eff} of partially molten rock is calculated as:

$$\rho_{eff} = \rho_{solid}(1 - M + M\frac{\rho_{0molten}}{\rho_{0soild}}) \quad (5)$$

where ρ_{0soild} and $\rho_{0molten}$ are the standard densities of solid and molten rock, respectively (see Table 1 in Zhu et al., 2013), and ρ_{solid} is the density of solid rocks at given *P* (MPa) and *T* (K) computed from:

$$\rho_{solid} = \rho_{0solid} \times [1 - (\alpha_{molten}M + \alpha_{solid}(1-M))(T - 298)] \times [1 - (\beta_{molten}M + \beta_{solid}(1-M))(P - 0.1)] \quad (6)$$

where α and β represent the thermal expansion and the compressibility of rocks (see Table 1 in Zhu et al., 2013). Due to the applied melt extraction, the actual density difference between solid and partially molten rocks is rather small in our models.

Rheological Model

The viscosity in our models depends on strain rate (defined in terms of deformation invariants), pressure and temperature according to standard experimentally determined flow laws (Ranalli, 1995) as:

$$\eta_{creep} = \left(\dot{\varepsilon}_{\mathrm{II}}\right)^{(1-n)/2n} (A_D)^{-1/n} \exp(\frac{E_a + PV_a}{nRT}) \quad (7)$$

where $\dot{\varepsilon}_{\mathrm{II}} = 1/2\,\dot{\varepsilon}_{ij}\dot{\varepsilon}_{ij}$ is the second invariant of the strain rate tensor, and A_D, E_a, V_a and n are experimentally determined flow law parameters (see Table 1 in Zhu et al., 2013).

The ductile rheology is combined with a brittle/plastic rheology to yield an effective visco-plastic rheology. For this purpose the Drucker-Prager yield criterion (Ranalli, 1995) is implemented by a limiting creep viscosity, η_{creep}, as follows:

$$\eta_{creep} \le \frac{c + P\sin(\varphi)}{\left(4\dot{\varepsilon}_{II}\right)^{1/2}} \quad (8)$$

where P is the complete (non-lithostatic) pressure (i.e., the mean stress), *c* is the cohesion (residual strength at *P* = 0), and φ is the effective internal friction angle (see Table 1 in Zhu et al., 2013). Assuming high pore fluid pressure in hydrated rocks (Gerya et al., 2008), the upper oceanic crust (basalts and sediments) are characterized by *c* = 1 MPa and sinφ = 0.

REFERENCES CITED

Bostock, M.G., Hyndman, R.D., Rondenay, S., and Peacock, S.M., 2002, An inverted continental Moho and serpentinization of the forearc mantle: Nature, v. 417, p. 536–538.

Burg, J.-P., and Gerya, T.V., 2005, Viscous heating and thermal doming in orogenic metamorphism: numerical modeling and geological implications: Journal of Metamorphic Geology, v. 23, p. 75–95.

Carlson, R.L., and Miller, D.J., 2003, Mantle wedge water contents estimated from seismic velocities in partially serpentinized peridotites: Geophysical Research Letters, v. 30, p. 1250, doi:10.1029/2002gl016600.

Connolly, J.A.D., 2005, Computation of phase equilibria by linear programming: A tool for geodynamic modeling and its application to subduction zone decarbonation: Earth and Planetary Science Letters, v. 236, p. 524–541.

Connolly, J.A.D., Schmidt, M.W., Solferino, G., and Bagdassarov, N., 2009, Permeability of asthenospheric mantle and melt extraction rates at mid-ocean ridges: Nature, v. 462, p. 209–214.

Elliott, T., Plank, T., Zindler, A., White, W., and Bourdon, B., 1997, Element transport from slab to volcanic front at the Mariana arc: Journal of Geophysical Research, v. 102, p. 14,991–15,019.

Faccenda, M., Gerya, T.V., and Burlini, L., 2009, Deep slab hydration induced by bending related variations in tectonic pressure: Nature Geoscience, v. 2, p. 790–793.

Faccenda, M., Gerya, T.V., Mancktelow, N.S., and Moresi, L., 2012, Fluid flow during slab unbending and dehydration: Implications for intermediate-depth seismicity, slab weakening and deep water recycling: Geochemistry Geophysics Geosystems, v. 13, p. Q01010, doi:10.1029/2011GC003860.

Faul, U.H., 2001, Melt retention and segregation beneath mid-ocean ridges: Nature, v. 410, p. 920–923.

Gerya, T.V., and Meilick, F.I., 2011, Geodynamic regimes of subduction under an active margin: effects of rheological weakening by fluids and melts: Journal of Metamorphic Geology, v. 29, p. 7–31.

Gerya, T.V., and Yuen, D.A., 2003, Rayleigh-Taylor instabilities from hydration and melting propel “cold plumes” at subduction zones: Earth and Planetary Science Letters, v. 212, p. 47–62.

Gerya, T.V., Connolly, J.A.D., and Yuen, D.A., 2008, Why is terrestrial subduction one-sided?: Geology, v. 36, p. 43–46.

Gerya, T.V., Connolly, J.A.D., Yuen, D.A., Gorczyk, W., and Capel, A.M., 2006, Seismic implications of mantle wedge plumes: Physics of the Earth and Planetary Interiors, v. 156, p. 59–74.

Gorczyk, W., Willner, A.P., Gerya, T.V., Connolly, J.A.D., and Burg, J.-P., 2007, Physical controls of magmatic productivity at Pacific-type convergent margins: numerical modelling: Physics of the Earth and Planetary Interiors, v. 163, p. 209–232.

Hall, P.S., and Kincaid, C., 2001, Diapiric flow at subduction zones: A recipe for rapid transport: Science, v. 292, p. 2472–2475.

Hawkesworth, C.J., Turner, S.P., McDermott, F., Peate, D.W., and van Calsteren, P., 1997, U/Th isotopes in arc magmas: implications for element transfer from the subducted crust: Science, v. 276, p. 551–555.

Hebert, L.B., Antoshechkina, P., Asimow, P., and Gurnis, M., 2009, Emergence of a low-viscosity channel in subduction zones through the coupling of mantle flow and thermodynamics: Earth and Planetary Science Letters, v. 278, p. 243–256.

Katz, R.F., Spiegelman, M., and Langmuir, C.H., 2003, A new parameterization of hydrous mantle melting: Geochemistry Geophysics Geosystems, v. 4, 1073, doi:10.1029/2002GC000433.

Kelley, K.A., Plank, T., Grove, T.L., Stolper, E.M., Newman, S., and Hauri, E., 2006, Mantle melting as a function of water content beneath back-arc basins: Journal of Geophysical Research, v. 111, p. B09208, doi:10.1029/2005jb003732.

Li, Z., Gerya, T.V., and Burg, J.P., 2010, Influence of tectonic overpressure on P-T paths of HP-UHP rocks in continental collision zones: Thermomechanical modelling: Journal of Metamorphic Geology, v. 28, p. 227–247.

Nikolaeva, K., Gerya, T.V., and Connolly, J.A.D., 2008, Numerical modelling of crustal growth in intraoceanic volcanic arcs: Physics of the Earth and Planetary Interiors, v. 171, p. 336–356.

Nikolaeva, K., Gerya, T.V., and Marques, F.O., 2011, Numerical analysis of subduction initiation risk along the Atlantic American passive margins: Geology, v. 39, p. 463–466.

Peacock, S.M., 1990, Fluid processes in subduction zones: Science, v. 248, p. 329–337.

Ranalli, G., 1995, Rheology of the Earth. 2nd ed Chapman & Hall.

Schmeling, H., et al., 2008, A benchmark comparison of spontaneous subduction models – towards a free surface: Physics of the Earth and Planetary Interiors, v. 171, p. 198–223.

Spiegelman, M., and McKenzie, D., 1987, Simple 2-D models for melt extraction at mid-ocean ridges and island arcs: Earth and Planetary Science Letters, v. 83, p. 137–152.

Vogt, K., Gerya, T.V., and Castro, A., 2012, Crustal growth at active continental margins: Numerical modeling: Physics of the Earth and Planetary Interiors, v. 192, p. 1–20.

Whitmarsh, R.B., Manatschal, G., and Minshull, T.A., 2001, Evolution of magma-poor continental margins from rifting to seafloor spreading: Nature, v. 413, p. 150–154.

Zhu, G., Gerya, T.V., Yuen, D.A., Honda, S., Yoshida, T., and Connolly, J.A.D., 2009, 3-D dynamics of hydrous thermalchemical plumes in oceanic subduction zones: Geochemistry Geophysics Geosystems, v. 10, p. Q11006, doi:10.1029/2009gc002625.

Zhu, G., Gerya, T.V., Honda, S., Tackley, P.J., and Yuen, D.A., 2011, Influence of the buoyancy of Partially molten rock on 3-D plume patterns and melt productivity above retreating slabs: Physics of the Earth and Planetary Interiors, v. 185, p. 112–121.

Zhu, G., Gerya, T.V., Tackley, P.J., and Kissling, E., 2013, Four-dimensional numerical modeling of crustal growth at active continental margins: Journal of Geophysical Research, v. 118, doi:10.1002/jgrb.50357.

Table DR1. Properties of model layers.

Layer	Flow law	Thickness (km)	Density (kgm^{-3})
Air	10^{18} Pa s	12	1
Upper Continental Crust	Wet Quartzite	33	2700
Lower Continental Crust	Wet Quartzite	12	2900
Continental Mantle	Wet Olivine	35	3250
Water	10^{18} Pa s	3	1000
Oceanic Crust	An75	8	3100
Oceanic Mantle	Wet Olivine	77	3300
Asthenosphere	Wet Olivine	The remaining to 200 km	3300

Table DR2. Model parameters.

Model	Density Contrast (kg/m3)	Thickness Continental Crust (km)	Thickness Continental Mantle (km)	Total Thickness Continental Lithosphere (km)	Total Depth Continental Lithosphere (km)	Temperature at base of Continental Lithosphere (K)	□ (°)	□ (°)
1	50	45	35	80	92	1619	0	45
2	50	45	35	80	92	1619	20	45
3	50	45	35	80	92	1619	40	45

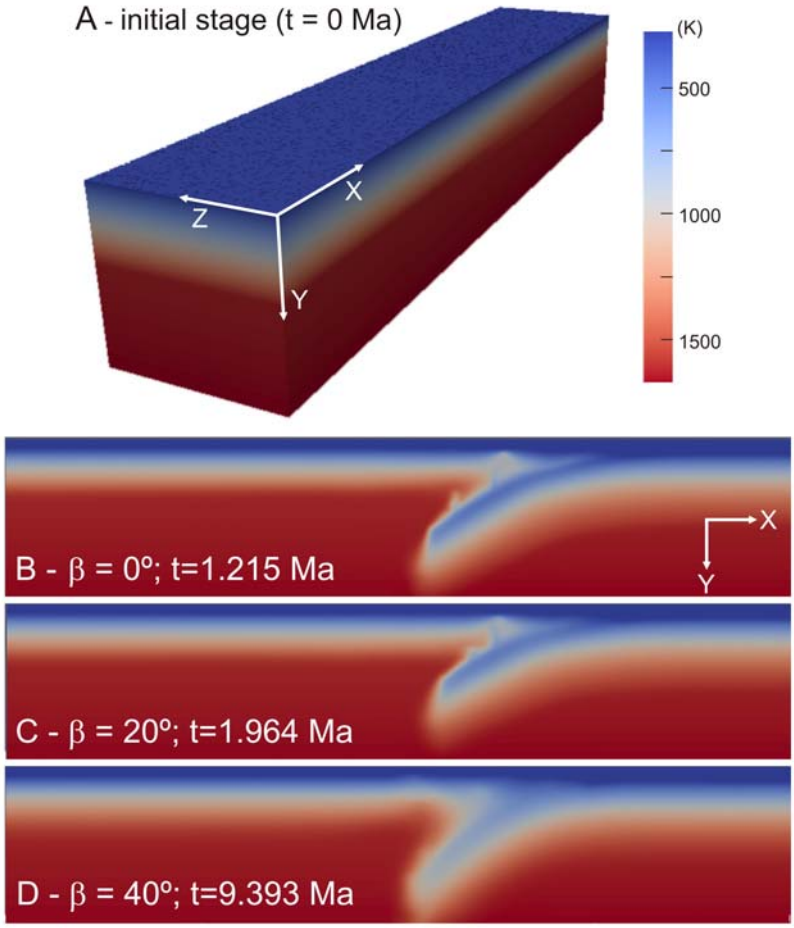

Figure DR1. Color maps representing the model temperatures in the initial stage (A), and at the front wall in the last stage of Models 1, 2 and 3. Note the higher temperature, from B to D, in the core of the sinking slab.

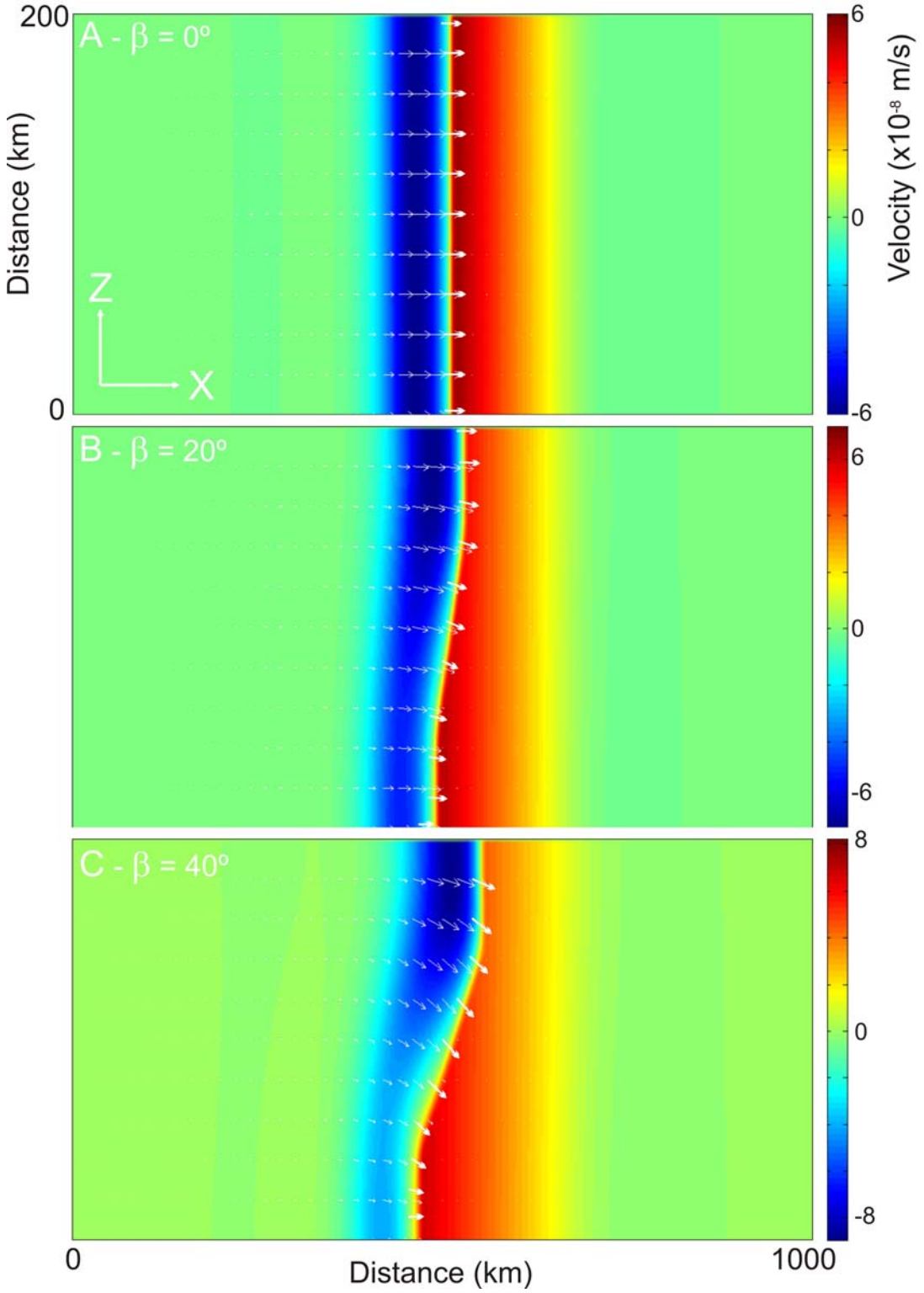

Figure DR2. *xz* plots of the velocity field. In color the *y* component, and as vectors (white arrows) the *xz* component. A, B and C for Models 1, 2 and 3 respectively. Note the great incorporation of the *z* component, towards the front wall (bottom), from A to C. Zero in A, as expected for a 2-D equivalent model, and maximum in C. Positive and negative values in the scale bar mean downward and upward flows, respectively.